Highly Coherent and Multi-Octave Mid-Infrared Supercontinuum Generations in a Reverse-Strip AlGaAs Waveguide with the Three Zero-Dispersion Wavelengths

YUJUN CHENG,[1,5] JINTAO LAI,[1,5] JINHUI YUAN,[1,2,6] CHAO MEI,[2] XIAN ZHOU,[2] QIANG WU,[3,4,7] BIN LIU,[4] BINBIN YAN,[1] KUIRU WANG,[1] CHONGXIU YU,[1] AND XINZHU SANG[1]

[1]*State Key Laboratory of Information Photonics and Optical Communications, Beijing University of Posts and Telecommunications, Beijing 100876, China*
[2]*Research Center for Convergence Networks and Ubiquitous Services, University of Science & Technology Beijing, Beijing 100083, China*
[3]*Department of Physics and Electrical Engineering, Northumbria University, Newcastle upon Tyne, NE1 8ST, United Kingdom*
[4]*Key Laboratory of Nondestructive Test (Ministry of Education), Nanchang Hangkong University, Nanchang 330063, China*
[5]*These authors contributed equally*
[6]*yuanjinhui81@bupt.edu.cn*
[7]*qiang.wu@northumbria.ac.uk*

Abstract: In this paper, a reverse-strip AlGaAs waveguide with the three zero-dispersion wavelengths (ZDWs) is designed. The corresponding three ZDWs are located at 3.74, 6.56, and 8.89 μm, respectively. The nonlinearity coefficient of the proposed reverse-strip AlGaAs waveguide is calculated as 2.09 $W^{-1}m^{-1}$ at wavelength 4.9 μm. The effects of the pump pulse parameters, waveguide length, and noise coefficient on the nonlinear dynamics of the supercontinuum (SC) generation are investigated. When the hyperbolic secant pump pulse with wavelength of 4.9 μm, peak power of 900 W, and duration of 100 fs is launched into the proposed waveguide and propagated after a 3 mm length, the highly coherent and multi-octave mid-infrared (MIR) SC spanning from 2.2 to 14.5 μm (more than 2.7 octaves, at -40 dB level) is generated. Finally, a possible fabrication process of the reverse-strip AlGaAs waveguide is introduced. Our research results have important applications in the MIR photonics, MIR spectroscopy, optical precision measurement, etc.

1. Introduction

Supercontinuum generations (SCGs) spanning from the visible to near-infrared spectral region in the optical waveguides have been extensively investigated [1-7]. Recently, the SCGs in MIR spectral region have received lots of research interests due to their potential applications in molecular spectroscopy [8], gas sensing [9], medical diagnostics [10], etc. At present, some nonlinear materials including silicon and chalcogenide as the optical waveguide materials have been explored for generating the MIR SCs. Lau et al. reported the SCG on a silicon chip, spanning from the communication band of ~1.5 μm to MIR spectral region beyond 3.6 μm [11]. In 2018, Karim et al. demonstrated the MIR SCG covering from 3.5 to 15 μm in a 20 mm long As_2Se_3 channel waveguide by using the pump source at wavelength 6 μm with the input peak power of 10 kW [12]. In 2019, Sinobad et al. reported an octave-spanning MIR SC source spanning from 2.63 to 6.18 μm by launching a pulse with peak power of 2.35 kW into a 7 cm long Si-Ge waveguide [13]. In 2020, Montesinos-Ballester et al. showed a two-octave MIR SCG on a 5.5 mm long Ge-rich graded

Si-Ge waveguides by using a pulse with 4.6 kW as the pump source [14].

Compared with the silicon and chalcogenide, GaAs, which is usually used as the substrate material in the laser devices, has remarkable advantages because of its larger nonlinear refractive index (~ 1.59×10^{-13} cm^2/W) [15] and wider transparency window (up to 20 μm) [16]. In 2014, Pigeon et al. reported the SCG spanning from 2 to 20 μm in a 67 mm-long GaAs crystal by using a CO_2 laser with center wavelength of 10.6 μm [17]. However, for the bulk GaAs crystal, the undesirable self-focused filament occurs easily. Moreover, the threshold power for the SCG can be very high, so the repetition rate of the used laser source has to be very low (~kHz), which is difficult to achieve for the commercially available lasers. These disadvantages make it difficult to use the generated SC as the practical light source for the traditional Fourier transform infrared spectroscopy. AlGaAs is an alloy of GaAs and AlAs. Compared with the GaAs crystal, the key advantage of AlGaAs is that its linear refractive index can be flexibly adjusted by changing the contents of Al and Ga in the alloy. Thus, the dispersion profile of the AlGaAs-based waveguide can be easily engineered. In addition, because the AlAs has the wide transmission spectral range from 0.6 to 15 μm [18], the AlGaAs is also expected to have a wide transparency window. In 2019, Chiles et al. demonstrated the SCG spanning from 2.3 to 6.5 μm in a suspended AlGaAs waveguide [19]. In 2020, Kuyken et al. achieved the octave-spanning coherent SCG in the wavelength range from 1.055 to 2.155 μm in an AlGaAs-on-insulator waveguide [20].

The bandwidth and coherence are the two key parameters for evaluating the SC performance. From the previous works, the dispersion characteristic of the optical waveguide has an important effect on the bandwidth and coherence of the generated SC [21-30]. The dispersion tailoring can be achieved through choosing the waveguide materials, designing the waveguide structure, and adjusting the waveguide geometry parameters [31-38]. When the low and flat dispersion profile with the multiple zero-dispersion wavelengths (ZDWs) is achieved over a broad wavelength range, the phase-matching nonlinear effects can occur, and the SCs with large bandwidth and good coherence could be generated.

In this paper, a reverse-strip AlGaAs waveguide with the three ZDWs of 3.74, 6.56, and 8.89 μm is designed. The low and flat dispersion profile is achieved in the considered wavelength range. We also investigate the effects of the pump pulse parameters, waveguide length, and noise coefficient on the SCG. By using the waveguide proposed, the multi-octave and highly coherent MIR SC spanning from 2.2 to 14.5 μm (more than 2.7 octaves, at -40 dB level) is generated when the hyperbolic secant pump pulse with wavelength of 4.9 μm, peak power of 900 W, and duration of 100 fs is propagated after a 3 mm length. It can be found that the lower peak power and shorter waveguide length are needed for the SCG in the designed reverse-strip AlGaAs waveguide compared with other waveguide platforms [12, 14]. Finally, a possible fabrication process of the reverse-strip AlGaAs waveguide using the plasma dry etching technology and chemical vapor deposition technology is introduced.

2. Theoretical model

The propagation dynamics of the short pulse in the AlGaAs waveguide can be modelled by the modified generalized nonlinear Schrödinger equation (GNLSE) as following [39]

$$\frac{\partial A(z,t)}{\partial z}+\frac{\alpha}{2}A(z,t)-\sum_{m\geq 2}\frac{i^{m+1}\beta_m(\omega)}{m!}\frac{\partial^m A(z,t)}{\partial t^m}=i\left(\gamma(\omega_0)+i\gamma_1(\omega_0)\frac{\partial}{\partial t}\right)\times\left[A(z,t)\int_0^\infty R(t')\left|A(z,t-t')\right|^2 dt'\right], \quad (1)$$

where $A(z, t)$ is the electrical field amplitude, α is the linear loss coefficient of the waveguide, $\beta_m(\omega)$ is the m-th order dispersion coefficient calculated from the Taylor expansion of the propagation constant, t is the retarded time, $\gamma(\omega_0)$ is the nonlinear coefficient at the center frequency ω_0, and $\gamma_1(\omega)$ is the first-order derivative of $\gamma(\omega)$. $\gamma(\omega)$ depends on the nonlinear refractive index n_2 and effective mode area $A_{eff.}$, which can be described as

$$\gamma = \frac{2\pi n_2}{\lambda A_{eff}} = \frac{2\pi}{\lambda} \frac{\iint n_2(x,y) |\overrightarrow{F(x,y)}|^4 \, dxdy}{(\iint |\overrightarrow{F(x,y)}|^2 \, dxdy)^2}, \tag{2}$$

$\overrightarrow{F(x,y)}$ represents for the transverse distribution of the optical field [40]. The relation between $\gamma_1(\omega)$ and $\gamma(\omega_0)$ is given by [39]

$$\frac{\gamma_1(\omega_0)}{\gamma(\omega_0)} = \frac{1}{\omega_0} + \left(\frac{1}{n_2(\omega)} \left(\frac{dn_2(\omega)}{d\omega} \right) \right)_{\omega-\omega_0} - \left(\frac{1}{A_{eff}(\omega)} \left(\frac{dA_{eff}(\omega)}{d\omega} \right) \right)_{\omega-\omega_0}, \tag{3}$$

Since n_2 of $Al_{0.18}Ga_{0.82}As$ changes a little after wavelength 1600 nm [41], the frequency dependence of $n_2(\omega)$ can be neglected. In this work, n_2 is taken as 1×10^{-17} m^2/W. When an $Al_{0.8}Ga_{0.2}As$ waveguide is used as the lower cladding material, α is equal to 0.5 dB/cm [42]. The last term of the right hand in Eq. (1) represents the instantaneous and delayed third-order nonlinear effects, including the self-phase modulation (SPM), Raman effect, and self-steeping. $R(t)$ has the following form

$$R(t) = (1 - f_R)\delta(t) + f_R h_R(t), \tag{4}$$

where Raman response function $h_R(t)$ can be described as

$$h_R(t) = \frac{\tau_1^2 + \tau_2^2}{\tau_1 \tau_2^2} \exp\left(-\frac{t}{\tau_2}\right) \sin\left(\frac{t}{\tau_1}\right), \tag{5}$$

where $\tau_1 = 18.72\times10^{-15}$ and $\tau_2 = 750\times10^{-15}$ are the inverses of the phonon oscillation frequency and bandwidth of the Raman gain spectrum, respectively [43]. The fractional Raman response f_R is found to be 0.047 [44].

The degree of the first-order coherence $g_{12}^{(1)}$ can be evaluated from the classical formula

$$g_{12}^{(1)}(\lambda) = \frac{\langle E_1^*(\lambda) E_2(\lambda) \rangle}{\sqrt{\langle |E_1(\lambda)|^2 \rangle \langle |E_2(\lambda)|^2 \rangle}}, \tag{6}$$

where $E(\lambda)$ denotes the spectral amplitude. The noise can be described as

$$n = \eta \hat{N} e^{i2\pi\hat{U}}, \tag{7}$$

where $\hat{N}$ is a normal distributed random variable with the mean value of 0 and standard deviation of 1. $\hat{U}$ is a uniformly distributed random variable between 0 and 1. The noise factor η describes the noise amplitude of the input pulse. In order to quantify the coherence of the SC more intuitively, two other factors are calculated as

$$R = \frac{\int_0^\infty |g_{12}^{(1)}(\lambda)| P(\lambda) d\lambda}{\int_0^\infty P(\lambda) d\lambda}, \tag{8}$$

$$K = \lg(1 - R). \tag{9}$$

where R as the weighted degree of coherence can measure the averaged coherence in the whole spectrum, and $P(\lambda)$ describes the ensemble average power spectrum of the generated SC [45, 46]. In Eq. (9), K is used to enlarge the detail of R when the coherence of the generated SC is close to 1.

3. Waveguide structure and characteristics

Fig. 1(a) shows the structure of the designed reverse-strip AlGaAs waveguide, where the top-cladding is air. From Fig. 1(a), the core and substrate materials of the waveguide are $Al_{0.18}Ga_{0.82}As$ and $Al_{0.8}Ga_{0.2}As$, respectively. The width of the core is W, the height of the core embedded in the substrate is H_d, and the height of the core exposed to the air is H_u. The quasi-TE mode field distributions calculated at wavelengths 3, 5, 7, 9, 12, and 15 μm are shown in Fig. 1(b) when the geometric structure parameters of the waveguide W, H_u, and H_d are chosen as 6, 0.7, and 1.4 μm, respectively. It should be pointed out that the thickness of

the substrate is selected as 6 μm in the simulation. It can be seen from Fig. 1(b) that most of the mode field energy can be well confined in the waveguide core at the considered wavelengths.

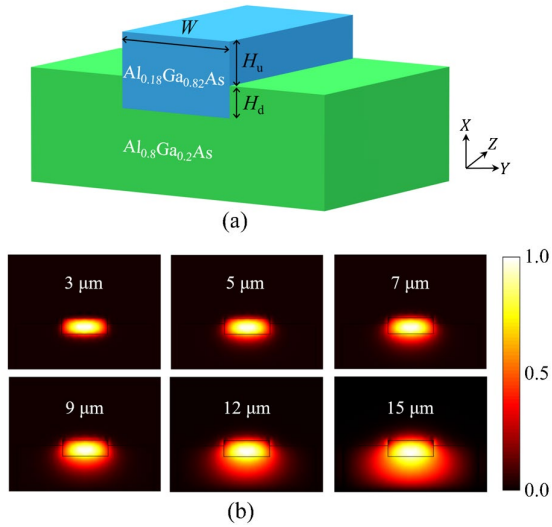

Fig. 1. (a) The structure of the proposed reverse-strip AlGaAs waveguide. (b) The mode filed distributions of the quasi-TE mode calculated at wavelengths 3, 5, 7, 9, 12, and 15 μm, respectively, when W = 6 μm, H_u = 0.7 μm, and H_d = 1.4 μm.

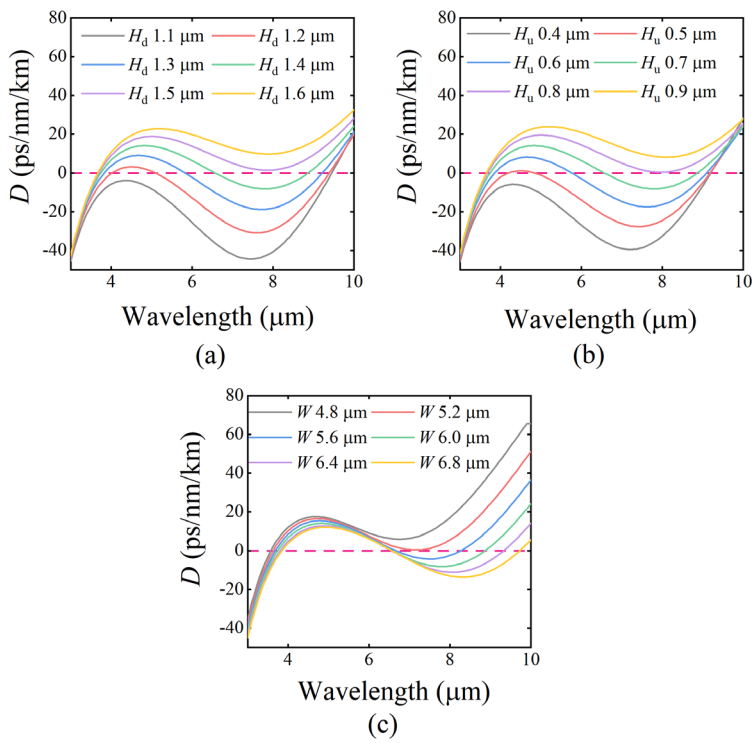

Fig. 2. The dispersion curves of the quasi-TE mode calculated as functions of wavelength when (a) H_d, (b) H_u, and (c) W are changed, respectively.

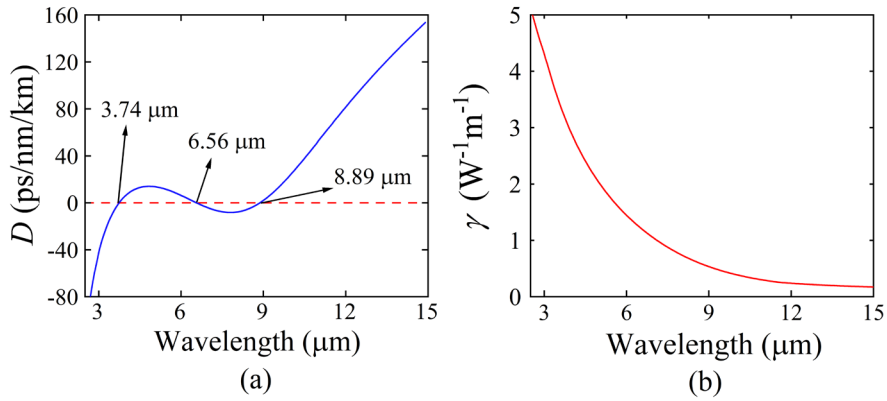

Fig. 3. (a) The dispersion curve of quasi-TE mode calculated as functions of wavelength, along with the three ZDWs of 3.74, 6.56, and 8.89 μm, and (b) the nonlinear coefficient γ calculated as functions of wavelength.

Table 1. The dispersion coefficient β_m calculated at wavelength 4.9 μm.

m	β_m
2	-0. 1801 ps^2/m
3	7.3813×10^{-4} ps^3/m
4	2.9958×10^{-5} ps^4/m
5	-5.0993×10^{-7} ps^5/m
6	5.1635×10^{-10} ps^6/m
7	-2.7913×10^{-10} ps^7/m
8	2.5971×10^{-11} ps^8/m
9	3.5379×10^{-13} ps^9/m
10	-7.8861×10^{-14} ps^{10}/m
11	1.5407×10^{-15} ps^{11}/m
12	5.2536×10^{-17} ps^{12}/m

The dispersion of the proposed waveguide can be obtained by the effective refractive index of the guided mode [47]. With the full-vector finite element method, the dispersion characteristic of the waveguide designed can be simulated. In order to investigate the sensitivity of the dispersion to the geometric parameters of the waveguide, Figs. 2(a)-2(c) show the dispersion curves of the quasi-TE mode calculated as functions of wavelength when H_d, H_u, and W are changed, respectively. From Figs. 2(a) and 2(b), as H_d and H_u increase, the dispersion curve occurs to move up. From Fig. 2(c), the dispersion curve occurs to red-shift with the increase of W. When 1.1 μm < H_d < 1.5 μm, 0.4 μm < H_u < 0.8 μm, and W > 5.2 μm, the dispersion curve has the three ZDWs. There is no potential to achieve more than three ZDWs through changing the H_d, H_u, and W unless some extra designs are considered [34]. In order to obtain a low and flat dispersion curve with multiple ZDWs, the geometry parameters of the waveguide are chosen as W = 6 μm, H_u, = 0.7 μm, and H_d = 1.4 μm, respectively, and the optimized dispersion curve of the quasi-TE mode is shown in Fig. 3(a). From Fig. 3(a), the dispersion value changes between -8.2 and 14.0 ps/nm/km in the wavelength range from 3.74 to 8.89 μm, and the low and flat dispersion profile is achieved, along with the three ZDWs of 3.74, 6.56, and 8.89 μm, respectively. The three ZDWs can divide the dispersion curve into the different dispersion regions, where the normal and anomalous dispersion regions are located in the wavelength range from 3.74 to 6.56 μm and 6.56 to 8.89 μm, respectively. The presence of the third ZDW creates a rich phase-matching topology, which is beneficial to the generation of SC [48]. Moreover, the calculated nonlinear coefficient γ of the

waveguide are also shown in Fig. 3(b). It can be seen from Fig. 3(b) that γ is calculated as 2.09 $W^{-1}m^{-1}$ at wavelength 4.9 μm. As shown in Table 1, up to 12-th order dispersion coefficients of the quasi-TE mode at wavelength 4.9 μm are considered in the following simulation.

4. Simulation results and discussion

By numerically solving Eq. (1) using the Runge-Kutta algorithm, the nonlinear dynamics of SCG in the proposed reverse-strip AlGaAs waveguide can be studied. When the wavelength is longer than 1.5 μm, the two-photon absorption (TPA) effect of $Al_{0.18}Ga_{0.82}As$ can be neglected [49]. Moreover, when the wavelength is longer than 2.2 μm, the three-photon absorption (3PA) effect of $Al_{0.18}Ga_{0.82}As$ can be beyond consideration [50]. In order to optimize the performance of the generated SC, we will investigate the effects of the pump pulse parameters on the SCG.

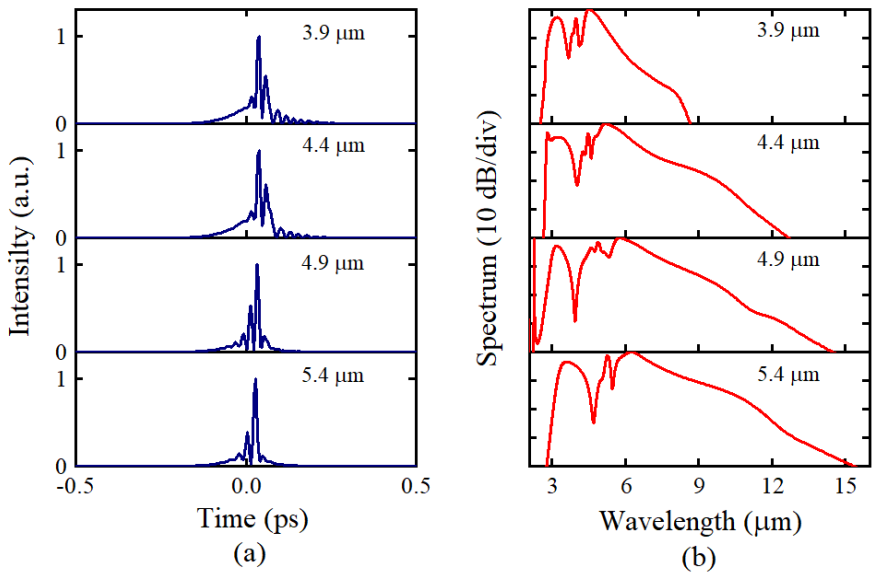

Fig. 4. (a) and (b) show the temporal and spectral expansions with different pump wavelengths in the proposed reverse-strip AlGaAs waveguide. The pump peak power is 900 W, pump duration is 100 fs, and pump wavelengths are chosen as 3.9, 4.4, 4.9, and 5.4 μm, respectively.

A hyperbolic secant pump pulse with peak power of 900 W and duration of 100 fs is launched into the designed reverse-strip AlGaAs waveguide. When center wavelength of the pump pulse is increased from 3.9 to 5.4 μm, the simulation results of the temporal and spectral evolutions in 3-mm long AlGaAs waveguide are shown in Figs. 4(a) and 4(b), respectively. From Figs. 4(a) and 4(b), some split peaks are observed when the pump wavelength is increased, accompanying with a narrower temporal pulse. The corresponding optical spectrum is gradually broadened when the center wavelength is increased from 3.9 to 4.9 μm due to the enhanced dispersion with the increase of β_2. The spectral broadening mechanisms is considered as following. Because the first ZDW of the waveguide is located at 3.74 μm, the pump pulse works in the anomalous dispersion region. The higher-order soliton (the calculated soliton order N = 10) will be formed because of the interplay between the negative dispersion and SPM. Under the effects of the higher-order dispersion and intrapulse Raman scattering, the higher-order soliton splits into the fundamental solitons and occurs to red-shift. During the process, the blue-shifted dispersion waves (DWs) are generated at the shorter wavelength side when the resonance matching condition is satisfied (calculated at wavelength around 3 μm) [51]. The red-shift process of the soliton will be suppressed by the

existing second ZDW (6.56 μm) [52]. At this time, the cross-phase modulation (XPM) effect between the residual pump, soliton, and DWs can further broaden the optical spectrum through generating the new spectral components at the shorter and longer wavelength sides. In addition, the spectral broadening may be enhanced by the four-wave mixing (FWM) effect due to the existing third ZDW (8.89 μm). When center wavelength of the pump pulse is located at 4.9 μm, the -40 dB bandwidth of the generated SC spans from 2.2 to 14.5 μm (more than 2.7 octaves). In contrast, when the center wavelength of the pump pulse is increased to 5.4 μm, the overall optical spectrum moves toward the longer wavelength side without obvious further broadening. The main reason is considered that the red-shifted soliton is suppressed because the wavelength of 5.4 μm is close to the second ZDW. Considering the small difference between the SCs generated by the pump pulses at wavelengths 4.9 μm and 5.4 μm and the difficulty in obtaining the longer wavelength pump sources, we choose 4.9 μm as the optimized pump center wavelength in the following investigations.

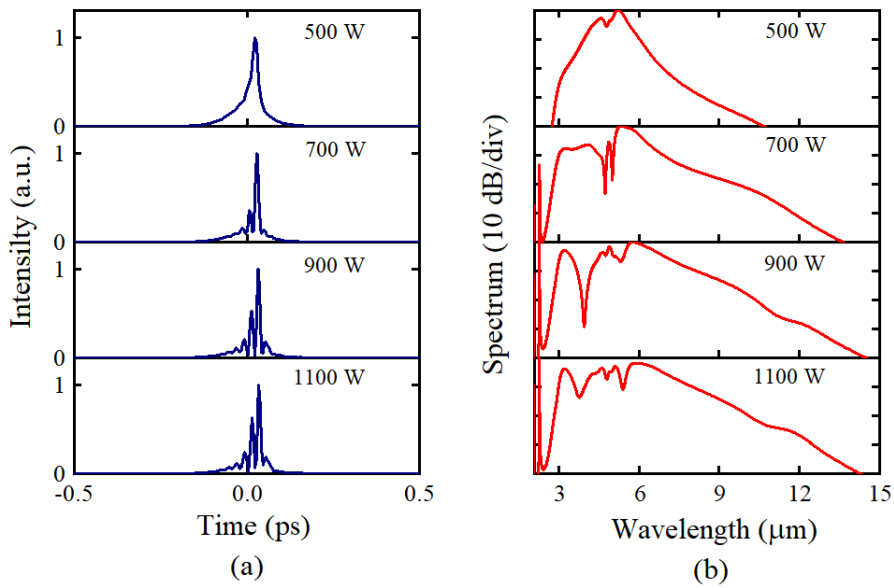

Fig. 5 (a) and (b) show the temporal and spectral expansions with different pump peak powers in the proposed reverse-strip AlGaAs waveguide. The pump wavelength is 4.9 μm, pump duration is 100 fs, and pump peak powers are chosen as 500, 700, 900, and 1100 W, respectively.

The influence of pump peak power on the SCG is studied. The simulation results of the temporal and spectral evolutions are shown in Figs. 5(a) and 5(b), respectively. For all cases, the pump wavelength is 4.9 μm and duration is 100 fs, and the peak power is increased from 500 to 1100 W. These power levels will not damage the facet of the used waveguide [19]. From Figs. 5(a) and 5(b), the pulse duration gradually becomes narrower when the peak power is increased. Remarkably, the peaks occur to split when peak power exceeds 700 W. The corresponding optical spectrum is broadened obviously. When peak power of the pump pulse is chosen as 500 W, the spectral broadening is dominated by the SPM effect. As peak power of the pump pulse increases to 700 and 900 W, the soliton dynamics and XPM effect play important role, and the optical spectrum is further broadened. Especially when peak power increases up to 900 W, the generated MIR SC can be more than 2.7 octaves (from 2.2 to 14.5 μm). As peak power of the pump pulse is further increased to 1100 W, the spectrum becomes flat and has not been further broadened. Considering that the spectral bandwidth exceeding 2.7 octaves and the kilowatt level peak power being easy to damage the waveguide, we choose 900 W as the optimized pump peak power.

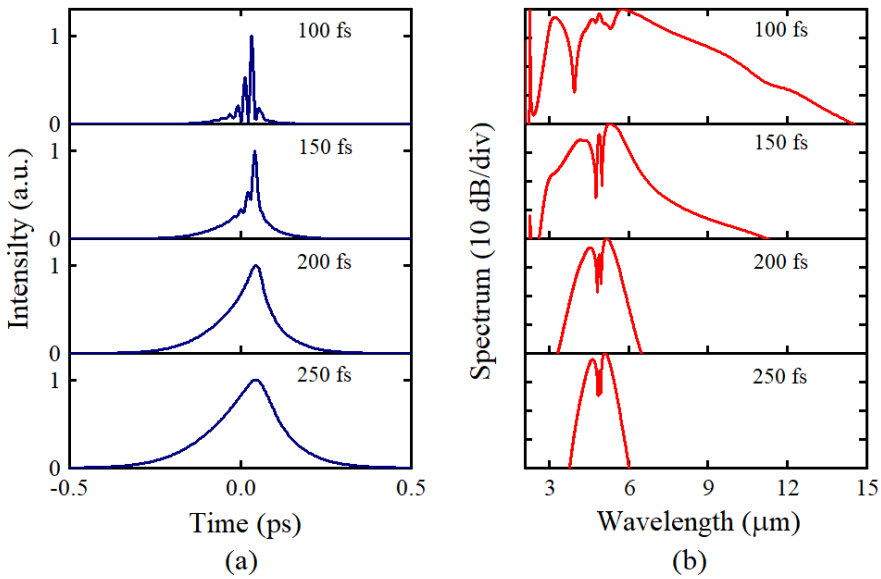

Fig. 6. (a) and (b) show the temporal and spectral expansions with different pump durations in the proposed reverse-strip AlGaAs waveguide. The pump wavelength is 4.9 μm, pump peak power is 900 W, and pump durations are chosen as 100, 150, 200, and 250 fs, respectively.

To determine the appropriate pump duration, 100, 150, 200, and 250 fs are chosen to investigative the nonlinear evolution dynamics in a 3-mm long waveguide, as shown in Figs. 6(a) and 6(b), respectively. It can be seen from Fig. 6(a) that as duration of the pump pulse increases from 100 to 250 fs, the pulse duration gradually becomes wide, and the split peaks gradually disappear when duration of the pump pulse is larger than 200 fs. As pump duration increases, the bandwidth of the generated SC decreases obviously, as shown in Fig. 6(b). The main reason is considered as following. As pump pulse duration increases, the pulse energy is increased, and the initial bandwidth gradually becomes narrower. The narrower initial bandwidth may cause the number of frequency components participated in the initial SPM stage less than the shorter duration pulse with a larger initial bandwidth, so the larger pump pulse duration will limit the broadening of spectrum. The largest bandwidth of the generated SC can be up to more than 2.7 octaves when the pulse duration of 100 fs is used. Therefore, 100 fs is the best choice for the pump pulse duration.

In conclusion, a hyperbolic secant pulse with center wavelength of 4.9 μm, peak power of 900 W, and duration of 100 fs is chosen as the pump source. In the following, the nonlinear dynamics for SCG under different waveguide lengths will be investigated. When the waveguide lengths are 2, 3, 4, and 5 mm, the temporal and spectral profiles at the output end of the designed reverse-strip AlGaAs waveguide are shown in Figs. 7(a) and 7(b), respectively. The temporal pulse becomes narrower, and split peaks appear when waveguide length is 3 mm, as shown in Fig. 7(b). When the waveguide length is increased from 3 to 5 mm, the pulse duration gradually becomes wider. It can be seen from Fig. 7(b) that when the waveguide length is changed from 2 to 3 mm, the spectral bandwidth is increased. However, the continuous broadening is not observed after the waveguide length of 3 mm, and the spectral flatness becomes worse. This is mainly due to the fact that at initial propagation, the SPM, soliton fission, XPM broadens the optical spectrum. When the waveguide length is longer than 3 mm, the accumulated dispersion and increased propagation loss degrade the spectral flatness and restrict the extension of the optical spectra.

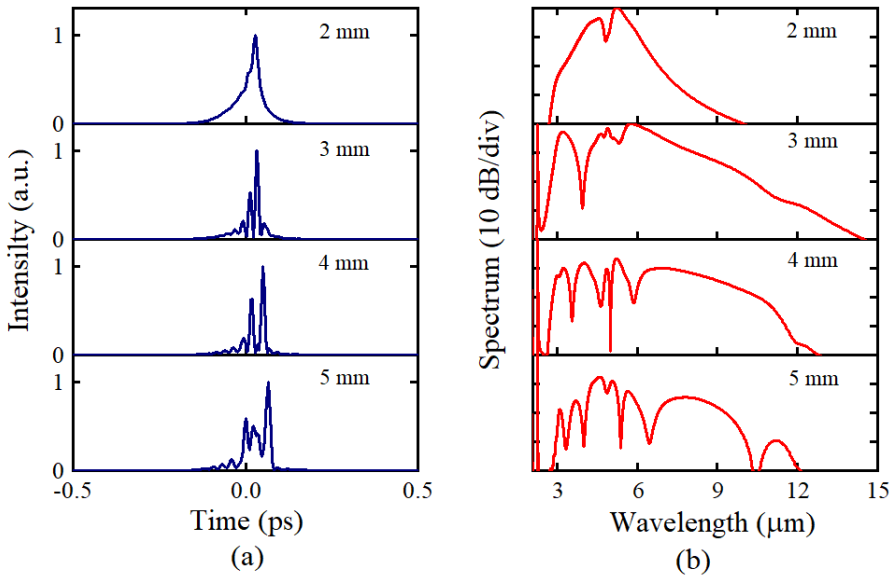

Fig. 7. (a) and (b) show the temporal and spectral expansions with different waveguide lengths in the proposed reverse-strip AlGaAs waveguide. The pump wavelength is 4.9 μm, pump peak power is 900 W, and pump duration is 100 fs. The waveguide lengths are chosen as 2, 3, 4, and 5 mm, respectively.

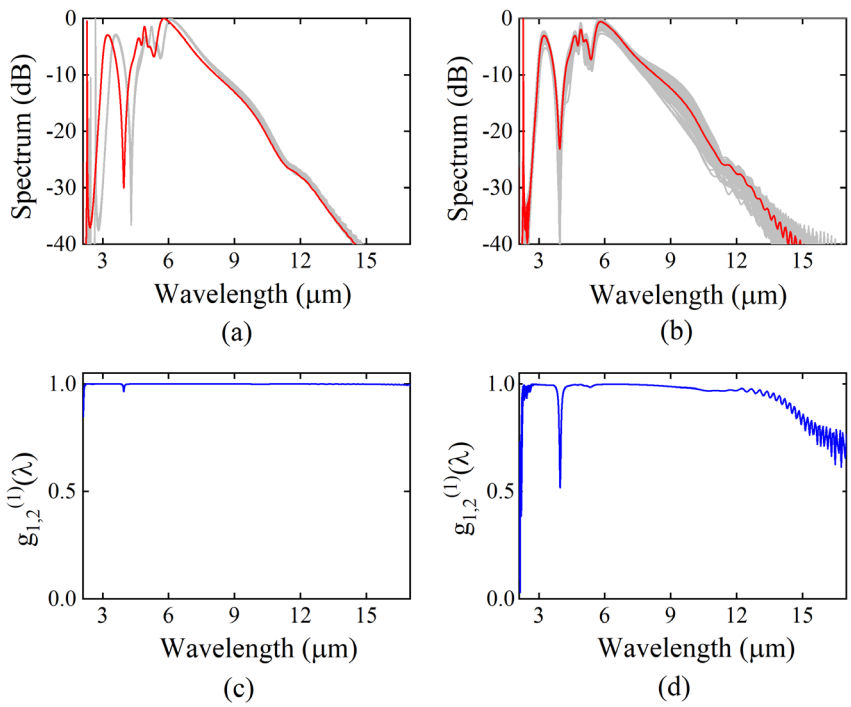

Fig. 8. (a) Spectral profiles and (c) $g_{12}^{(1)}$ of the SC generated at the output end of the designed reverse-strip AlGaAs waveguide with η = 0.0001. (b) Spectral profiles and (d) $g_{12}^{(1)}$ of the SC generated at the output end of the designed reverse-strip AlGaAs waveguide with η = 0.01. The grey and red lines in (a) and (b) represent the overlapped spectra of the 50 shots and average values of the 50 shots, respectively.

Finally, we will investigate the effect of noise on SCG in the proposed waveguide. Figs. 8(a) and 8(b) show the averaged spectra (red lines) and overlapped spectra (gray lines) of 50 shots for the same pump condition and waveguide length when η is chosen as 0.0001 and 0.01, respectively. The spectral fluctuation in Fig. 8(a) is very slight while the spectral fluctuation in Fig. 8(b) becomes very obvious. Figs. 8(c) and 8(d) show the calculated $g_{12}^{(1)}$ with 50 shots when η = 0.0001 and η = 0.01, respectively. It can be seen from Figs. 8(c) and 8(d) that in the considered wavelength range, $g_{12}^{(1)}$ is equal to 1 when η = 0.0001. In contrast, $g_{12}^{(1)}$ is seriously degraded when η = 0.01. In order to quantitatively compare the value of coherence for different η, the weighted degree R as a function of lg(η) in the whole spectra is shown in Fig. 9(a). It can be seen from Fig. 9(a) that when lg(η) ≤ -3 ($\eta \leq 0.001$), R is close to 1. However, R drops quickly from 1 to 0.49 as lg(η) increases from -3 to -1 (that is, η increases from 0.001 to 0.1). In Fig. 9(b), K as a function of lg(η) is also calculated since R is very close to 1. In Fig. 9(b), K is increased with increasing lg(η). Therefore, good coherence of the generated SC can be obtained when lg(η) ≤ -3 ($\eta \leq 0.001$).

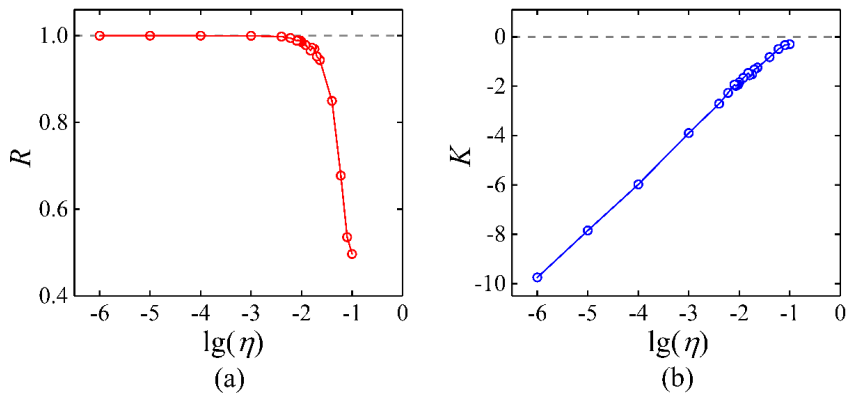

Fig. 9. The weighted degree of coherence (a) R and (b) K calculated in the whole spectra versus the random noise level lg(η) for the generated SC.

By optimizing the pump parameters, waveguide length, and η, multi-octave and highly coherent MIR SC can be obtained. When pump pulse with center wavelength of 4.9 μm, peak power of 900 W, and duration of 100 fs is launched into the proposed reverse-strip AlGaAs waveguide with a length of 3 mm and η is chosen as 0.0001, the temporal and spectral evolutions of the pump pulse along the waveguide length are shown in Figs. 10(a) and 10(b), respectively. Correspondingly, the bottom and top in Figs. 10(a) and 10(b) also show the temporal and spectral profiles at the input and output ends of the reverse-stripe AlGaAs waveguide, respectively. From Fig. 10(a), with the increase of waveguide length, pulse becomes narrower gradually. The pulse occurs to split starting at the waveguide length of 2 mm. In Fig. 10(b), the optical spectrum is symmetrically broadened by SPM when the waveguide is shorter than 2 mm. After the wavelength length of 2 mm, the soliton dynamics and XPM effect make the optical spectrum further extend toward the shorter and longer wavelength sides. What's more, because of the existence of the third ZDW at 8.89 μm, the FWM effect may further enhance the spectral broadening at the longer wavelength side. Fig. 10(c) shows the evolution of $g_{12}^{(1)}$ along the waveguide length. It can be seen from Fig. 10(c) that $g_{12}^{(1)}$ is always remains 1 in the considered wavelength range, showing a good coherence of generated SCs. The main reason is considered that the modulation instability could be effectively depressed by the relatively small β_2. Therefore, with the designed reverse-strip AlGaAs waveguide, we can generate the multi-octave and highly coherent MIR SC, whose -40 dB bandwidth spans from 2.2 to 14.5 μm (more than 2.7 octaves).

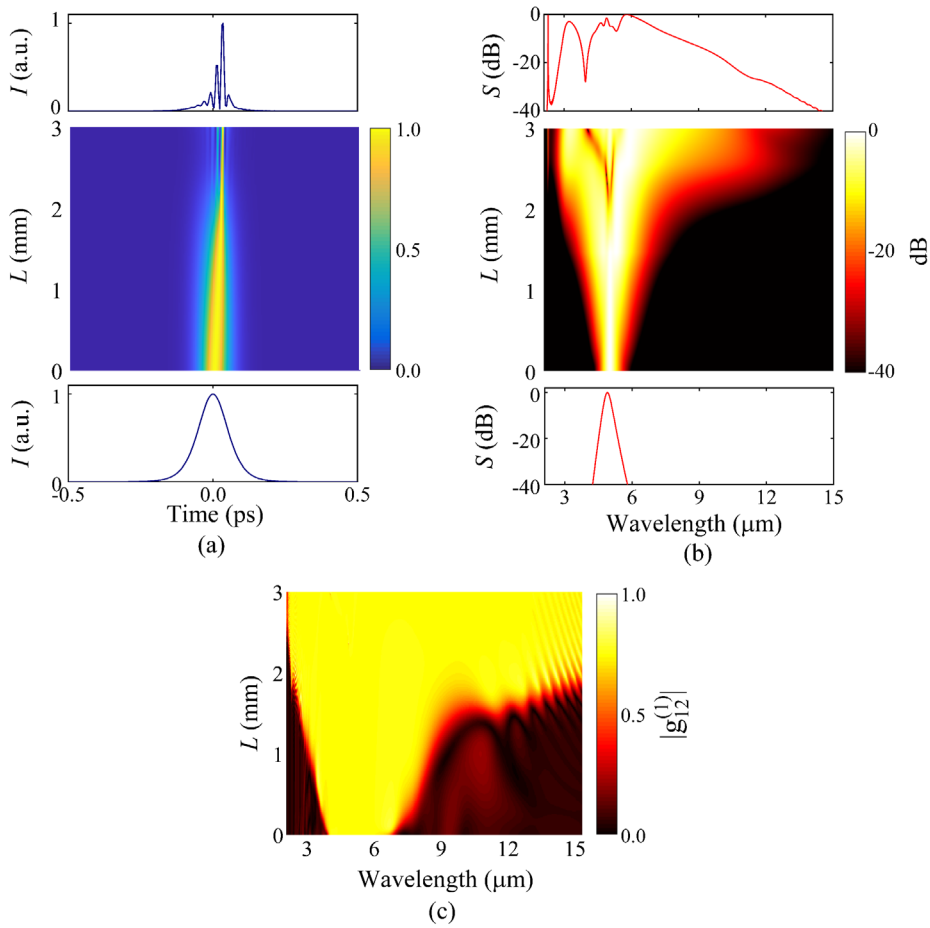

Fig. 10. (a) and (b) show the temporal and spectral evolutions along the waveguide length, respectively, the bottom and top figures showing the temporal and spectral profiles at the input and output ends of the designed reverse-strip AlGaAs waveguide. *I* in (a) represents the intensity. *S* in (b) represents the spectrum. (c) shows the evolution of $g_{12}^{(1)}$ along the waveguide length.

At present, the plasma etching technology and atmospheric chemical vapor deposition technology can be used to fabricate the proposed reverse-strip waveguide [53]. Figs. 11(a)-11(f) show the possible essential fabrication process of the proposed waveguide. First, the surface of the $Al_{0.8}Ga_{0.2}As$ substrate was cleaned and covered with a layer of SiN mask by the plasma enhanced chemical vapor deposition (PECVD) [Figs. 11(a) and 11(b)] [19, 54]. Second, a micro-trench was fabricated by ultraviolet lithographic patterning and plasma dry etching [Figs. 11(c) and 11(d)]. Third, a $Al_{0.18}Ga_{0.82}As$ layer was grown on the trench with the PECVD technology [Fig. 11(e)]. Finally, the reverse-strip waveguide was formed by using the phosphoric acid to remove the SiN mask [Fig. 11(f)].

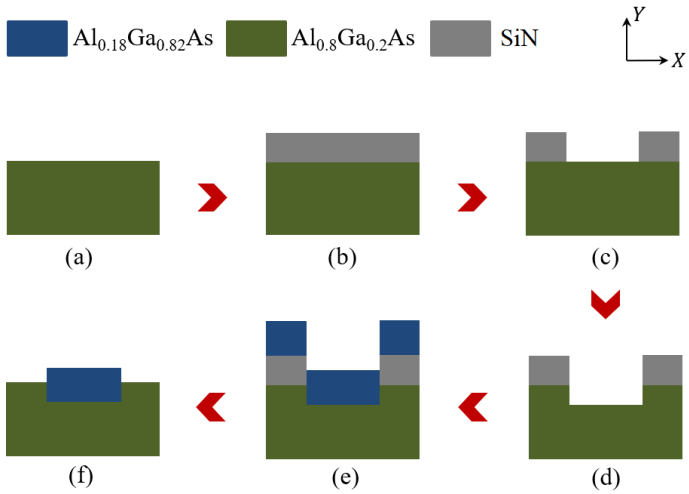

Fig. 11. A possible fabrication process of the proposed reverse-strip AlGaAs waveguide.

5. Conclusions

In summary, we design a reverse-strip AlGaAs waveguide with the three ZDWs for generating the MIR SC. The effects of the pump pulse parameters, waveguide length, and η on the SCG are investigated. The MIR SC with good coherence and more than 2.7 octaves (at -40 dB level) is obtained with the designed reverse-strip AlGaAs waveguide when a hyperbolic secant pulse with center wavelength of 4.9 μm, peak power of 900 W, and duration of 100 fs is used as the pump source. In addition to generating such a broadband SC, the designed reverse-strip AlGaAs waveguide itself shows more solid and simpler fabrication process when compared with the suspended structure of AlGaAs on silicon waveguides proposed in ref. [19]. The proposed waveguide also can generated polarization-insensitive SC by changing the H_d, H_u, and W [55]. It is believed that our research results can find significant applications in the MIR photonics, MIR spectroscopy, optical precision measurement, etc.

Acknowledgement

This work was supported by the National Natural Science Foundation of China (61875238) and the BUPT Excellent Ph.D. Students Foundation under Grant CX2020319.

Disclosures

The authors declare that there are no conflicts of interest related to this article.

References

1. H. Hu, W. Li, and N. K. Dutta, "Supercontinuum generation in dispersion-managed tapered-rib waveguide," Appl. Opt. **52**(30), 7336-7341 (2013).
2. F. Lu and W. Knox, "Generation of a broadband continuum with high spectral coherence in tapered single-mode optical fibers," Opt. Exp. **12**(2), 347-353 (2004).
3. O. Fedotova, A. Husakou, and J. Herrmann, "Supercontinuum generation in planar rib waveguides enabled by anomalous dispersion," Opt. Exp. **14**(4), 1512-1517 (2006).
4. P. J. Johnson, V. I. Prokhorenko, and R. J. Miller, "Stable UV to IR supercontinuum generation in calcium fluoride with conserved circular polarization states," Opt. Exp. **17**(24), 21488-21496 (2009).
5. J. Swiderski and M. Michalska, "High-power supercontinuum generation in a ZBLAN fiber with very efficient power distribution toward the mid-infrared," Opt. Lett. **39**(4), 910-913 (2014).
6. H. Saghaei and V. Van, "Broadband mid-infrared supercontinuum generation in dispersion-engineered silicon-on-insulator waveguide," J. Opt. Soc. Am. B. **36**(2), A193-A202 (2019).

7. A. R. Johnson, A. S. Mayer, A. Klenner, K. Luke, E. S. Lamb, M. R. E. Lamont, C. Joshi, Y. Okawachi, F. K. Wise, M. Lipson, U. Keller, and A. L. Gaeta, "Octave-spanning coherent supercontinuum generation in a silicon nitride waveguide," Opt. Lett. **40**(21), 5117–5120 (2015).
8. A. Schliesser, N. Picqué, and T. W. Hänsch, "Mid-infrared frequency combs," Nat. Photon. **6**(7), 440-449 (2012).
9. P. M, F. Slemr and K. Maurer, "Near-and mid-infrared laser-optical sensors for gas analysis," Opt. Lasers Eng. **37**, 101-114 (2002).
10. B. J. Guo, Y. Wang, C. Peng, H. L. Zhang, G. P. Luo, H. Q. Le, C. Gmachl, D. L. Sivco, M. L. Peabody, and A. Y. Cho, "Laser-based mid-infrared reflectance imaging of biological tissues," Opt. Exp. **12**(1), 208-219 (2004).
11. R. K. Lau, M. R. Lamont, A. G. Griffith, Y. Okawachi, M. Lipson, and A. L. Gaeta, "Octave-spanning mid-infrared supercontinuum generation in silicon nanowaveguides," Opt. Lett. **39**(15), 4518-4521 (2014).
12. M. R. Karim, H. Ahmad, S. Ghosh, and B. M. A. Rahman, "Design of dispersion-engineered As_2Se_3 channel waveguide for mid-infrared region supercontinuum generation," J. Appl. Phys. **123**(21), 213101 (2018).
13. M. Sinobad, A. D. Torre, R. Armand, B. Luther-Davies, P. Ma, S. Madden, A. Mitchell, D. J. Moss, J. M. Hartmann, J.-M. Fedeli, C. Monat, and C. Grillet, "High Coherence at *f* and 2*f* of mid-infrared supercontinuum generation in silicon germanium waveguides," IEEE J. Sel. Top. Quantum Electron. **26**(2), 1-8 (2019).
14. M. Montesinos-Ballester, C. Lafforgue, J. Frigerio, A. Ballabio, V. Vakarin, Q. K. Liu, J. M. Ramirez, X. L. Roux, D. Bouville, A. Barzaghi, C. Alonso-Ramos, L. Vivien, G. Isella, and D. Marris-Morini, "On-Chip Mid-Infrared Supercontinuum Generation from 3 to 13 μm Wavelength," ACS Photonics, **7**(12), 3423–3429 (2020).
15. M. Dinu, F. Quochi, and H. Garcia, "Third-order nonlinearities in silicon at telecom wavelengths," Appl. Phys. Lett. **82**(18), 2954 (2003).
16. C. J. Johnson, G. H. Sherman, and R. Weil, "Far infrared measurement of the dielectric properties of GaAs and CdTe at 300 K and 8 K," Appl. Opt. **8**(8), 1667-1672 (1969).
17. J. J. Pigeon, S. Y. Tochitsky, C. Gong, and C. Joshi, "Supercontinuum generation from 2 to 20 μm in GaAs pumped by picosecond CO_2 laser pulses," Opt. Exp. **39**(11), 3246-3249 (2014).
18. M. J. Weber, Hand Book of Optical Materials. (CRC press, Berkeley, California, 2003).
19. J. Chiles, N. Nader, E. J. Stanton, D. Herman, G. Moody, J. G. Zhu, J. C. Skehan, B. Guha, A. Kowligy, J. T. Gopinath, K. Srinivasan, S. A. Diddams, I. Coddington, N. R. Newbury, J. M. Shainline, S. W. Nam, and R. P. Mirin, "Multifunctional integrated photonics in the mid-infrared with suspended AlGaAs on silicon," Optica **6**, 1246-1254 (2019).
20. B. Kuyken, M. Billet, F. Leo, K. Yvind, and M. H. Pu, "Octave-spanning coherent supercontinuum generation in an AlGaAs-on-insulator waveguide," Opt. Lett. **45**(3), 603-606 (2020).
21. Z. L. Li, J. H. Yuan, C Mei, F. Li, X. Zhou, B. B. Yan, Q. Wu, K. R. Wang, X. Z. Sang, K. P. Long, and C. X. Yu, "Multi-octave mid-infrared supercontinuum and frequency comb generation in a suspended As_2Se_3 ridge waveguide," Appl. Opt. **48**(31), 8404–8410 (2019).
22. J. H. Yuan, Z. Kang, F. Li, X. T. Zhang, X. Z. Sang, Q. Wu, B. B. Yan, K. R. Wang, X. Zhou, K. P. Zhong, G. Y. Zhou, C. X. Yu, C. Lu, H. Y. Tam, and P. K. A. Wai, "Mid-infrared octave-spanning supercontinuum and frequency comb generation in a suspended germanium-membrane ridge waveguide," J. Lightwave Technol. **35**(14), 2994–3002 (2017).
23. M. Sinobad, A. D. Torre, R. Armand, B. Luther-Davies, P. Ma, S. Madden, A. Mitchell, D. J. Moss, J.-M. Hartmann, J.-M. Fedeli, C. Monat, and C. Grillet, "Mid-infrared supercontinuum generation in silicon-germanium all-normal dispersion waveguides," Opt. Lett. **45**(18), 5008-5011 (2020).
24. C. Mei, J. H. Yuan, Z. Kang, F. Li, X. T. Zhang, B. B. Yan, X. Z. Sang, Q. Wu, X. Zhou, K. P. Zhong, L. Wang, K. R. Wang, C. X. Yu, and P. K. A. Wai, "Multi-octave mid-infrared supercontinuum generation in dispersion-engineered AlGaAs-based strip waveguides," 2016 15th International Conference on Optical Communications and Networks (ICOCN). IEEE, 2017.
25. M. R. Karim, B. M. Rahman, and G. P. Agrawal, "Mid-infrared supercontinuum generation using dispersion-engineered $Ge_{11.5}As_{24}Se_{64.5}$ chalcogenide channel waveguide," Opt. Exp. **23**, 6903–6914 (2015).
26. J. T. Lai, J. H. Yuan, Y. J. Cheng, C. Mei, X. Zhou, Q. Wu, B. B. Yan, K. R. Wang, K. P. Long, C. X. Yu, and X. Z. Sang, "Dispersion-engineered T-type germanium waveguide for mid-infrared supercontinuum and frequency comb generations in all-normal dispersion region," OSA Continuum **3**(9), 2320-2331 (2020).
27. H. Ahmad, M. R. Karlm, and B. M. A. Rahman, "Modeling of dispersion engineered chalcogenide rib waveguide for ultra-flat mid‑infrared supercontinuum generation in all‑normal dispersion regime," Appl. Phys. B **124**(3), 47 (2018).
28. T. S. Saini, N. P. T. Hoa, K. Nagasaka, X. Luo, T. H. Tuan, T. Suzuki, and Y. Ohishi, "Coherent mid-infrared supercontinuum generation using rib waveguide pumped with 200 fs laser pulses at 2.8 μm," Appl. Opt. **57**, 1689–1693 (2018).
29. F. Xu, J. H. Yuan, C. Mei, B. B. Yan, X. Zhou, Q. Wu, K. R. Wang, X. Z. Sang, C. X. Yu, and G. Farrell, "Highly coherent supercontinuum generation in a polarization-maintaining CS_2-core photonic crystal fiber". Appl. Opt. **58**(6), 1386-1392 (2019).
30. Y. J. Cheng, J. H. Yuan, C. Mei, F. Li, Z. Kang, B. B. Yan, X. Zhou, Q. Wu, K. R. Wang, X. Z. Sang, K. P. Long, C. X. Yu, and G. Farrell, "Self-similar picosecond pulse compression for supercontinuum generation at mid-infrared wavelength in silicon strip waveguides," Opt. Commun. **454**, 124380 (2020).

31. L. Zhang, Q. Lin, Y. Yue, Y. Yan, R. G. Beausoleil, and A. E. Willner, "Silicon waveguide with four zerodispersion wavelengths and its application in on-chip octave-spanning supercontinuum generation," Opt. Exp. **20**(2), 1685–1690 (2012).
32. L. Zhang, Y. Yue, R. G. Beausoleil, and A. E. Willner, "Flattened dispersion in silicon slot waveguides," Opt. Exp. **18**(19), 20529–20534 (2010).
33. L. Zhang, Y. Yan, Y. Yue, Q. Lin, O. Painter, R. G. Beausoleil, and A. E. Willner, "On-chip two-octave supercontinuum generation by enhancing self-steepening of optical pulses," Opt. Exp. **19**(12), 11584–11590 (2011).
34. Y. H. Guo, Z. Jafari, L. J. Xu, C. J. Bao, P. C. Liao, G. F. Li, A. M. Agarwal, L. C. Kimerling, J. Michel, A. E. Willner, and L. Zhang, "Ultra-flat dispersion in an integrated waveguide with five and six zero-dispersion wavelengths for mid-infrared photonics," Photonics Res. **7**(11), 1279-1286 (2019).
35. Y. H. Guo, J. Wang, Z. Han, K. Wada, L. C. Kimerling, A. M. Agarwal, J. Michel, Z. Zheng, G. F. Li, and L. Zhang, "Power-efficient generation of octave-spanning mid-IR frequency combs in a germanium," Nanophotonics **7**(8), 1461–1467 (2018).
36. L. Xu, X. Ni, B. Liu, Y. Li, and M. Hu, "Ultra-flat and low dispersion in a horizontal silicon nitride slot waveguide at near-infrared wavelengths," Opt. Eng. **55**(3), 037109 (2016).
37. Y. H. Guo, Z. Jafari, A. M. Agarwal, L. C. Kimerling, G. F. Li, J. Michel, and L. Zhang, "Bilayer dispersion-flattened waveguides with four zero dispersion wavelengths," Opt. Lett. **41**(21), 4939–4942 (2016).
38. Y. Zhang, H. Liu, Q. Sun, N. Huang, and Z. Wang, "Supercontinuum generation in strip/slot hybrid waveguide with flat and low dispersion," Appl. Opt. **54**(15), 4850–4856 (2015).
39. G. P. Agrawal, Nonlinear fiber optics, Fifth ed. (Academic Press, 2013).
40. J. Hu, C.R. Menyuk, and L.B. Shaw, "Computational study of 3–5 μm source created by using supercontinuum generation in As_2S_3 chalcogenide fibers with a pump at 2 μm," Opt. Lett. **35**(17), 2907–2909 (2010).
41. A. Villeneuve, C. C. Yang, G. I. Stegeman, C. H. Lin and H. H. Lin, "Nonlinear refractive-index and two-photon-absorption near half the band gap in AlGaAs," Appl. Phys. Lett. **62**(20), 2465-2467 (1993).
42. G. A. Porkolab, P. Apiratikul, B. Wang, S. H. Guo and C. J. K. Richardson, "Low propagation loss AlGaAs waveguides fabricated with plasma-assisted photoresist reflow," Opt. Exp. **22**(7), 7733 (2014).
43. O. K. Kim and W. G. Spitzer, "Infrared reflectivity spectra and Raman spectra of $Ga_{1-x}Al_xAs$ mixed crystals," J. Appl. Phys. **50**(6), 4362 (1979).
44. M. Sharma, V. Dhasarathan, J. S. Skibina, M. S. M. Rajan, S. Konar, T. T. Hoang, and Q. M. Ngo, "Giant nonlinear AlGaAs-Doped glass photonic crystal fibers for efficient soliton generation at femtojoule energy," IEEE Photon. J. **11**(4), 7102411-1-11 (2019).
45. F. Li, Q. Li, J. H. Yuan, P. K. A. Wai, "Highly coherent supercontinuum generation with picosecond pulses by using self-similar compression," Opt. Exp. **22**(22), 27339-27354 (2014).
46. G. Genty, M. Surakka, J. Turunen, and A. T. Friberg, "Complete characterization of supercontinuum coherence," J. Opt. Soc. Am. B. **28**(9), 2301-2309 (2011).
47. K. Saitoh and M. Koshiba, "Finite element beam propagation method with perfectly matched layers for anisotropic optical waveguides," J. Lightw. Technol. **19**(3), 405–413 (2001).
48. S. P. Stark, F. Biancalana, A. Podlipensky, and P. S. J. Russell, "Nonlinear wavelength conversion in photonic crystal fibers with three zero-dispersion points," Phys. Rev. A **83**(2), 023808 (2011).
49. S. Adachi, "GaAs, AlAs, and $Al_xGa_{1-x}As$ Material parameters for use in research and device applications," J. Appl. Phys. **58**(3), R1 (1985).
50. J. U. Kang, A. Villeneuve, M. Sheik-Bahae, G. I. Stegeman, K. Al-hemyari, J. S. Aitchison, and C. N. Ironside, "Limitation due to three-photon absorption on the useful spectral range for nonlinear optics in AlGaAs below half band gap," Appl. Phys. Lett. **65**(2), 147 (1994).
51. G. Q. Chang, L. J. Chen, and F. X. Kärtner. "Highly efficient Cherenkov radiation in photonic crystal fibers for broadband visible wavelength generation," Opt. Lett. **35**(14), 2361-2363 (2010).
52. D. V. Skryabin, F. Luan, J. C. Knight, and P. S. J. Russel, "Soliton self-frequency shift cancellation in photonic crystal fibers," Science **301**(5640), 1705-1708 (2003).
53. C. Li, P. Guo, W. Huang, W. Zhang, P. Xu, and P. Zhang, "Reverse-strip-structure $Ge_{28}Sb_{12}Se_{60}$ chalcogenide glass waveguides prepared by micro-trench filling and lift-off," J. Opt. Soc. Am. B **37**(1), 82-87 (2020).
54. I. Goykhman, U. Sassi, B. Desiatov, N. Mazurski, S. Milana, D. de Fazio, A. Eiden, J. Khurgin, J. Shappir, U. Levy, and A. C. Ferrari, "On-chip integrated, silicon-graphene plasmonic schottky photodector with high responsivity and avalanche photogain," Nano Lett. **16**(5), 3005-3013 (2016).
55. L. Q. Zhang, J. H. Yuan, Y. J. Cheng, C. Mei, J. T. Lai, X. Zhou, Q. Wu, B. B. Yan, K. R. Wang, C. X. Yu, and X. Z. Sang, "Polarization-insensitive reverse-ridge AlGaAs waveguide for the mid-infrared supercontinuum generation," Opt. Commun. **502**, 127407 (2022).